Finite Element Modeling of Railroad Track Components

Hailing Yu, and David Jeong

Volpe National Transportation Systems Center

Abstract: A ballasted railroad track consists of rails, fasteners, ties, ballast and the underlying subgrade. Realistic simulations of the track response to interactive vehicle-rail loads will require detailed models of each component. In this paper, finite element (FE) models are developed for some of the ballasted track components including wood and concrete crossties, ballast and subgrade. A user material subroutine is employed to predict the failure of wood ties based on an orthotropic stress criterion. The concrete tie is modeled as a heterogeneous medium with prestressing tendons embedded in a concrete matrix. The concrete material observes elasticity followed by damaged plasticity. The interfaces between the tendons and concrete are simulated with cohesive elements, and there can be initiation and evolution of damage to the bond between the steel tendons and concrete. Further, the granular and frictional ballast material is modeled with extended Drucker-Prager plasticity, and the subgrade is modeled as an elastic half space. All material parameters are obtained from the open literature.

The track component models are then assembled and applied in FE analyses. First, the stress states in concrete ties upon release of the pretention in the prestressing tendons are predicted. Second, individual wood and concrete tie responses to a simplified, uniformly distributed pressure load over the rail seats in a ballasted track are analyzed. The analyses indicate the failure modes in this type of loading as tensile cracking at the tie base below the rail seats of a concrete tie and compressive failure in the rail seats of a wood tie.

Future work will include developing and incorporating fastener and rail models in the track assembly. A complete track model will be subjected to more realistic vehicle-rail forces in FE analyses and expected to reproduce the complex stress states in the rail seats of a tie more accurately. Such analyses may provide a better understanding of the mechanisms responsible for the rail seat deterioration failures observed in some concrete ties.

Keywords: Railroad Track, Rail Seat Deterioration, Wood Crosstie, Concrete Crosstie, Ballast, Subgrade, Pretension Release, and Rail Seat Loading.

1. Introduction

Ties are an integral part of a railroad track system which also includes rails, rail pads, insulators, fasteners and ballast. The main functions of a railroad tie include supporting the rails and transferring rail forces to the ballast bed, maintaining track gauge and rail inclination, and insulating the rails electrically. Because of the relatively short service lives of timber ties, alternative tie materials such as concrete, steel and plastic composites have been employed or explored. In particular, concrete ties can be engineered to meet specific service requirements and add overall stability and performance to a railroad track structure. They were estimated to last twice as long as timber ties with the potential of lowered life cycle costs. These favorable

qualities led to great interests and the first major installation of prestressed concrete ties in North America in 1966 [1]. Figure 1 illustrates the dual block (or two block, twin block, Figure 1a) as well as the more widely used monoblock concrete crossties (Figure 1b).

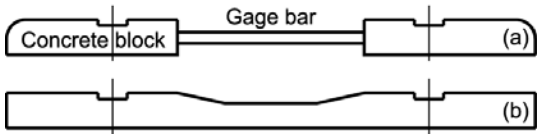

Figure 1. Illustration of concrete crossties: (a) dual block and (b) monoblock (reproduced from [1])

Despite the stated advantages, there have been concerns over unresolved performance issues of concrete ties that can lead to increased maintenance costs and shortened service lives. One of the concerns is the susceptibility of concrete ties to rail seat deterioration (RSD), a failure mode that has been increasingly observed in the northeast corridor and was believed to be responsible for an Amtrak passenger train derailment accident in Home Valley, Washington in 2005 [2]. To meet the full potential of concrete ties in high speed and heavy haul services, a better understanding of their behavior under dynamic loading is needed. Computational models have emerged as an inexpensive and flexible tool to study concrete tie behavior in a ballasted track. The objective of this research is to develop small scale, detailed finite element (FE) models for railroad concrete crossties and study the responses of individual ties to rail seat loading. Models at this scale accounts for the heterogeneity of concrete ties and involves explicit representations of the prestressing tendons and the concrete components [3] as well as their interfaces governed by bond-slip relationships [4, 5]. Such details allow the pretension release phase of the concrete tie manufacturing process to be simulated first, and the resulting stress state then serves as an initial condition as a concrete tie model is further subjected to rail seat loads. A wood tie model is also developed and subjected to the same type of rail seat loads. Wood and concrete crosstie performances are compared based on the FE simulations. Ballast and subgrade models are also included to provide the support conditions of a ballasted track.

2. Constitutive relations

The commercial FE analysis software Abaqus is employed in this study [6]. The constitutive relations of steel, concrete, concrete-tendon interface, wood, ballast and subgrade are needed in modeling and discussed in this section.

2.1 Steel

The prestressing steel is assumed to be linear elastic with a perfectly plastic yield strength. The Young's modulus is 30,000,000 psi and the Poison's ratio is 0.3. The steel material for the rail is assumed to be linear elastic with the same Young's modulus and Poisson's ratio.

2.2 Concrete

A damaged plasticity model is available for the concrete material. Concrete behaves differently in tension and in compression as illustrated by the stress-strain curves in uniaxial tension and compression, respectively, in Figure 2. In uniaxial tension, linear elasticity is followed by tension

stiffening (Figure 2a), and in uniaxial compression, linear elasticity is followed first by strain hardening and then by strain softening (Figure 2b). The compressive strength σ_{cu} is often one order of magnitude higher than the tensile strength σ_{t0}.

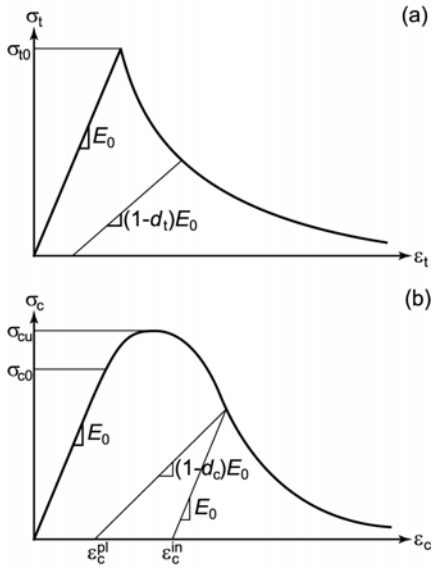

Figure 2. Concrete stress-strain responses to (a) uniaxial tension (σ_t-ε_t) and (b) uniaxial compression (σ_c-ε_c).

For linear elasticity, the stress-strain (σ_t-ε_t for tension and σ_c-ε_c for compression) relations for uniaxial stresses may be expressed as

$$\sigma_t = E_0\varepsilon_t, \varepsilon_t \le \sigma_{t0}/E_0 \tag{1}$$

$$\sigma_c = E_0\varepsilon_c, \varepsilon_c \le \sigma_{c0}/E_0 \tag{2}$$

where E_0 is the initial Young's modulus and σ_{c0} is the elastic or proportional limit in uniaxial compression.

For tension stiffening in uniaxial tension, a stress-displacement (σ_t-w_t) relation is adopted and expressed in a form modified from the exponential equation proposed in [7]

$$\sigma_t = \sigma_{t0}e^{-aw_t/w_{t0}}, \varepsilon_t > \sigma_{t0}/E_0 \tag{3}$$

where a and w_{t0} are constants to be determined. Apparently σ_t approaches 0 as $w_t \to \infty$. If we assume that w_{t0} corresponds to a sufficiently small σ_{tmin} such that

$$\sigma_t\Big|_{w_t=w_{t0}} = \sigma_{tmin} \tag{4}$$

and that the area under the σ_t-w_t curve up to w_t=w_{t0} is equal approximately to the fracture energy G_f needed to create a unit area of cracked surface [8]

$$\int_0^{w_{t0}} \sigma_t dw_t = G_f \tag{5}$$

then a and w_{t0} can be solved from Eqs. (3-5) as

$$a = \mathrm{Ln}\left(\sigma_{t0}/\sigma_{tmin}\right) \tag{6}$$

$$w_{t0} = \frac{G_f \mathrm{Ln}\left(\sigma_{t0}/\sigma_{tmin}\right)}{\sigma_{t0}\left(1-\sigma_{tmin}/\sigma_{t0}\right)} \tag{7}$$

The equation for the strain hardening in uniaxial compression is modified from the work referenced in [9-11] and expressed as

$$\sigma_c = \sigma_{c0} + \frac{E_0\varepsilon_c - \sigma_{c0}}{1 + A\left(\dfrac{E_0\varepsilon_c - \sigma_{c0}}{E_0\varepsilon_{c0} - \sigma_{c0}}\right)^n}, \frac{\sigma_{c0}}{E_0} < \varepsilon_c \le \varepsilon_{c0} \tag{8}$$

where A and n are constants to be determined and ε_{c0} is the strain corresponding to the maximum stress σ_{cu}

$$\sigma_c\Big|_{\varepsilon_c=\varepsilon_{c0}} = \sigma_{cu} \tag{9}$$

The derivative of the hardening curve is further assumed to reach zero at the peak stress

$$\frac{d\sigma_c}{d\varepsilon_c}\Big|_{\varepsilon_c=\varepsilon_{c0}} = 0 \tag{10}$$

Solving Eqs. (8-10) yields the hardening constants as follows

$$A = \frac{E_0\varepsilon_{c0} - \sigma_{c0}}{\sigma_{cu} - \sigma_{c0}} - 1 \tag{11}$$

$$n = 1 + \frac{1}{A} = \frac{E_0\varepsilon_{c0} - \sigma_{c0}}{E_0\varepsilon_{c0} - \sigma_{cu}} \tag{12}$$

Last, the strain softening behavior is assumed to follow the empirical equation proposed in [11] and referenced in [12]

$$\sigma_c = \frac{\sigma_{cu} r\, \varepsilon_c/\varepsilon_{c0}}{r - 1 + \left(\varepsilon_c/\varepsilon_{c0}\right)^{kr}}, \varepsilon_c > \varepsilon_{c0} \tag{13}$$

where r and k are empirical constants that can be calculated as

$$r = 0.8 + \sigma_{cu}/17 \tag{14}$$

$$k = 0.67 + \sigma_{cu}/62 \tag{15}$$

in which σ_{cu} is expressed in MPa.

At the tension stiffening or strain softening stages, concrete will unload according not to E_0 but to a degraded Young's modulus E. The tensile damage variable d_t and the compressive damage variable d_c are then introduced to define the degraded modulus in each case. The damage variable d_t in the uniaxial case may be defined according to Eq. (3) as

$$d_t(w_t) = 1 - e^{-aw_t / w_{t0}} \tag{16}$$

In uniaxial compression, the relationship between the plastic strain ε_c^{pl} and the inelastic strain ε_c^{in} (Figure 2b) is expressed as

$$\varepsilon_c^{pl} = \varepsilon_c^{in} - \frac{d_c}{1-d_c}\frac{\sigma_c}{E_0} \tag{17}$$

where ε_c^{pl} may assume the empirical form suggested in [13]

$$\varepsilon_c^{pl} = 0.166\frac{\varepsilon_c^2}{\varepsilon_{c0}} + 0.132\varepsilon_c \tag{18}$$

The damage variable d_c can then be calculated from Eqs. (13, 17-18) with any given ε_c.

An overall stiffness degradation variable d is further defined as a function of both d_t and d_c, and it indicates the damaged state of a material integration point (0: undamaged; 1: completely damaged). In addition to uniaxial relations, biaxial and triaxial behaviors are similarly defined. This damaged plasticity modeling for concrete is based on the original work by Lubliner et al. [14], which was further extended by Lee and Fenves [15] to account for the behavior under cyclic loads.

The concrete model parameters used in this study are summarized in Table 1 for σ_{cu}=7,000 psi. It is assumed that $\sigma_{t0}=0.085\sigma_{cu}$, $\sigma_{tmin}=0.01\sigma_{t0}$ and $\sigma_{c0}=0.6\sigma_{cu}$, based on the general literature on concrete properties and especially [7,15]. The non-derived parameters in Table 1 (G_f and ε_{c0}) are those of concrete specimens with an average uniaxial compressive strength of 6,364 psi in [7].

Table 1. Concrete model parameters.

E_0 (ksi)	ν	σ_{t0} (psi)	G_f (lbf/inch)	a	w_{t0} (inch)
4,631.5	0.2	595	0.322	4.605	2.517×10^{-3}

σ_{c0} (psi)	σ_{cu} (psi)	ε_{c0}	A	n	r	k
4,200	7,000	1.843×10^{-3}	0.5485	2.823	3.639	1.448

2.3 Concrete-Tendon Interfaces

Cohesive elements are used to model the concrete-strand or concrete-wire interfaces. Figure 3 illustrates a cohesive element with a negligible thickness. It has a local coordinate system where *n* is the normal direction and *s* and *t* are the shear directions. The corresponding traction components are t_n, t_s and t_t, respectively. Traction-displacement constitutive relations are adopted for the cohesive elements to model the interface behavior, that is, linear elasticity followed by damage initiation and evolution. There are four damage initiation criteria available: maximum

nominal stress and strain criteria and quadratic nominal stress and strain criteria. For instance, the quadratic nominal stress criterion is stated as

$$\left\{\frac{\langle t_n \rangle}{t_n^0}\right\}^2 + \left\{\frac{t_s}{t_s^0}\right\}^2 + \left\{\frac{t_t}{t_t^0}\right\}^2 = 1 \tag{19}$$

where $\langle \cdot \rangle$ is the Macaulay bracket, and t_n^0, t_s^0 and t_t^0 are the nominal normal and shear strengths, respectively, for the interface. Damage evolution can be displacement or energy based. We currently employ a displacement based exponential softening law.

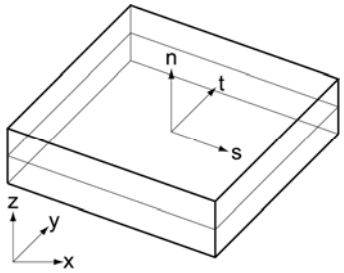

Figure 3. Illustration of a cohesive element (reproduced from [6])

The parameters needed for the interface modeling of concrete ties are the elastic stiffness *K*, the bond strength τ_0 (for the shear strengths) and the failure displacement u_0. With the lack of more appropriate data, the normal strength is assumed to be the same as the shear strength; this appears acceptable as the interfaces are unlikely to fail in the normal direction for the concrete tie applications. While there have been numerous references characterizing the bond-slip relations between concrete and its reinforcing bars, tendons or strands, there has been far less research on the bond properties of prestressing strands or wires in railroad ties. The average flexural bond strength obtained by Abrishami and Mitchell [16] for smooth seven-wire strands with a nominal 0.375 inch diameter is adopted. The same bond strength is assumed for the dented seven-wire strands or smooth single wires in this study; it is understood that this may not be accurate (see e.g, [17]) and that additional experimental study is merited to provide sufficient bond strength data for concrete ties. The current interface model parameters are *K*=24,000 lbf/inch, τ_0=701 psi and u_0=2 inches.

2.4 Wood

Wood is often characterized as an orthotropic material with which three perpendicular axes are attached: the longitudinal axis *L* parallel to the fiber (grain), the radial axis *R* normal to the growth rings, and the tangential axis *T* perpendicular to the fiber and tangent to the growth rings [18]. Twelve constants (nine of which are independent) may be used to define orthotropic elasticity: three moduli of elasticity *E*, three shear moduli *G* and six Poisson's ratios ν. The Poisson's ratio ν_{ij} ($i \neq j$ $i,j=L,R,T$) has the physical interpretation of the transverse strain in the *j*-direction when the material is stressed in the *i*-direction. In general, ν_{ij} and ν_{ji} are not the same, and they are interrelated by

$$\frac{\nu_{ij}}{E_i} = \frac{\nu_{ji}}{E_j} \tag{20}$$

The elastic constants define the elastic compliance according to the following equations

$$\begin{Bmatrix} \varepsilon_{LL} \\ \varepsilon_{RR} \\ \varepsilon_{TT} \\ \gamma_{LR} \\ \gamma_{LT} \\ \gamma_{RT} \end{Bmatrix} = \begin{bmatrix} \frac{1}{E_L} & \frac{-\nu_{RL}}{E_R} & \frac{-\nu_{TL}}{E_T} & 0 & 0 & 0 \\ \frac{-\nu_{LR}}{E_L} & \frac{1}{E_R} & \frac{-\nu_{TR}}{E_T} & 0 & 0 & 0 \\ \frac{-\nu_{LT}}{E_L} & \frac{-\nu_{RT}}{E_R} & \frac{1}{E_T} & 0 & 0 & 0 \\ 0 & 0 & 0 & \frac{1}{G_{LR}} & 0 & 0 \\ 0 & 0 & 0 & 0 & \frac{1}{G_{LT}} & 0 \\ 0 & 0 & 0 & 0 & 0 & \frac{1}{G_{RT}} \end{bmatrix} \begin{Bmatrix} \sigma_{LL} \\ \sigma_{RR} \\ \sigma_{TT} \\ \sigma_{LR} \\ \sigma_{LT} \\ \sigma_{RT} \end{Bmatrix} \tag{21}$$

Further, tensile, compressive and shear strengths for an orthotropic wood material can be denoted as follows

Table 2. Orthotropic strength limits

Symbol	Description
X_{Lt}	Tensile strength in the fiber direction *L*
X_{Lc}	Compressive strength in the fiber direction *L*
X_{Rt}	Tensile strength in the radial direction *R*
X_{Rc}	Compressive strength in the radial direction *R*
X_{Tt}	Tensile strength in the tangential direction *T*
X_{Tc}	Compressive strength in the tangential direction *T*
S_{LR}	Shear strength in the *L*-*R* plane
S_{LT}	Shear strength in the *L*-*T* plane
S_{RT}	Shear strength in the *R*-*T* plane

A user material subroutine is adopted and determines that if any of the strength quantities are reached in their corresponding material directions, the material is considered failed.

The material properties of the white oak species in the wood handbook [18] were employed in the current study and summarized in Table 3.

Table 3: Wood material parameters based on the white oak species [18]

E_L (psi)	E_R (psi)	E_T (psi)	ν_{LR}	ν_{LT}	ν_{RT}	G_{LR} (psi)	G_{LT} (psi)	G_{RT} (psi)
1,958,000	319,154	140,976	0.369	0.428	0.618	168,388	158,598	41,118

X_{Lt} (psi)	X_{Lc} (psi)	X_{Rt}, X_{Tt} (psi)	X_{Rc}, X_{Tc} (psi)	S_{LR}, S_{LT} (psi)
15,200	7,440	800	1,070	2,000

2.5 Ballast and Subgrade

The Extended Drucker-Prager model is applied to the ballast material. It is a plasticity model suitable for simulating granular, frictional materials. The main parameters used are Young's modulus (30,168 psi), Poisson's ratio (0.3) and yield strength (58 psi). A quick parameter study by increasing the yield strength to 100 psi shows only small differences in the predicted tie response. Similar modeling work for railroad ballast can be found in [19].

The subgrade is modeled as an elastic half space. Its Young's modulus (72,519 psi) and Poisson's ratio (0.25) are adopted from [20].

3. Finite element model

The macroscopic heterogeneity of a concrete crosstie is modeled as shown in Figure 4. The geometry of concrete, strands/wires and their interfaces are explicitly represented and assigned the respective constitutive relations described above. The schematic of a full model including ballast and subgrade is shown in Figure 5. With reference to a global track system, the *x*-axis corresponds to the longitudinal rail direction, *y*-axis to the vertical direction and *z*-axis to the transverse direction. The concrete tie may be replaced with the homogeneous and orthotropic wood tie model to study the wood tie behavior. The ballast and subgrade are modeled for a distance corresponding to one tie spacing along the longitudinal or *x*-direction. The subgrade is bounded by a hemicylindrical layer of infinite elements intended to simulate the infinite nature of the subgrade support. Infinite elements are assigned appropriately selected decay functions for their basic solution variables, and they are employed in conjunction with standard finite elements to model the far field [21]. The tie spacing is assumed to be 30 inches for concrete ties and 19 inches for wood ties, and the ballast depth is 24 inches in this study.

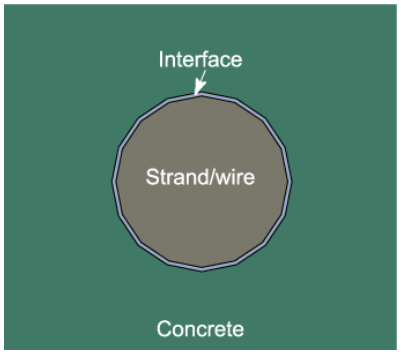

Figure 4. Macroscopic heterogeneity in concrete tie modeling: concrete, a strand/wire and their interface.

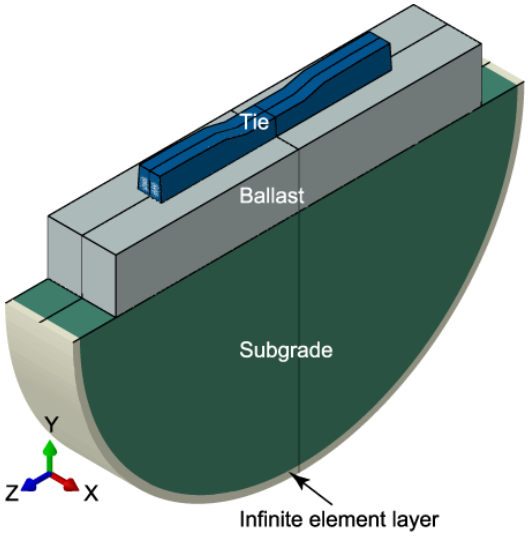

Figure 5. Modeling of an individual crosstie sitting on ballast and subgrade bounded by an infinite element layer.

Two railroad concrete crossties are studied here, one with eight prestressing strands and the other with twenty four prestressing wires. The indented seven-wire strands have a nominal diameter of 0.375 inches, whereas the single wires have a nominal diameter of 0.207 inches. Compared to the 8-strand tie, the 24-wire tie increases the bonding surface area by 65.6% while reducing the steel volume by 8.6%. With assumed quarter symmetries in both the geometry and the loading, only one fourth of the schematic shown in Figure 5 is considered in FE modeling. Figure 6 shows the typical quarter symmetric FE meshes for the 8-strand and 24-wire concrete crossties.

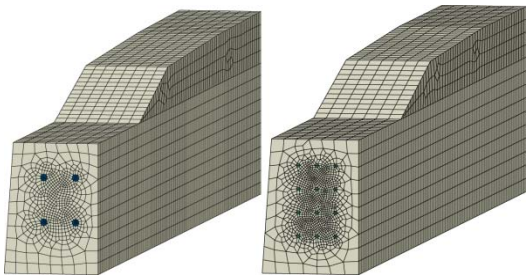

Figure 6. Typical quarter symmetric FE meshes for the 8-strand and 24-wire concrete crossties.

The wood tie is assumed to have the same length as those of the concrete ties (102 inches), a width of 9 inches and a depth of 7 inches. The material properties are assumed to follow those of the white oak species defined above. A steel plate is used to cover the rail seat area.

Roller boundary conditions are applied on the symmetric planes to enforce the symmetric conditions. In addition, the ballast and subgrade models span a length equal to one tie spacing in the *x*- or longitudinal rail direction, and their *y*-*z* surfaces bounding the FE domains are also

assigned roller boundary conditions to account for the infinite structures that continue along the *x*-direction.

The tendons are assigned initial pretensions according to specifications. These prestresses are then released in the simulations to yield the initial stress and strain states in concrete ties before any additional loading may be applied. These simulations are conducted as a static analysis step. Further, as illustrated in Figure 7, uniformly distributed pressure loads are applied directly on predefined rail seat areas. The simulation of this loading scenario is conducted as a dynamic analysis step.

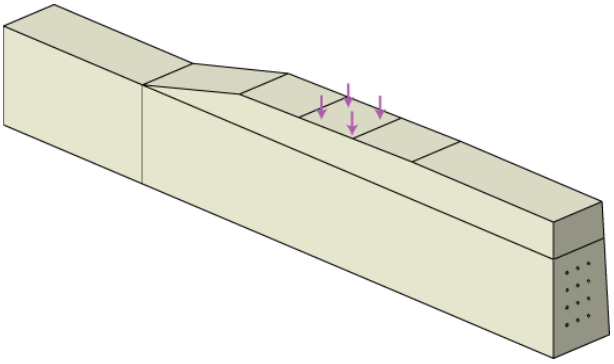

Figure 7. Illustration of uniformly distributed pressure loads applied directly on a predefined rail seat area.

4. Results

The results obtained from the FE analyses of the pretension release phase are presented and compared for the 8-strand and 24-wire ties. The FEA results of the rail seat loading cases are compared for both concrete ties and the wood tie.

4.1 Pretension Release

The initial pretension release is first simulated, and it results in tie deformations, some degree of interface deterioration toward the tie ends, compressive stress and strain states in the concrete and losses of pretensions in the tendons. Figure 8 shows the deformation profiles of the 8-stand and 24-wire crossties after pretension release. Figure 9 shows the contours of interface deterioration *D*, of which the main observations are: (1) the interfaces remain intact for most parts of the ties (bluish contours with D=0), (2) there are interface deteriorations toward the ends of the ties (greenish contours with D>0), and (3) interface deteriorations are more limited in extent for the 24-wire tie than for the 8-strand tie.

Figure 10 shows the contours of the minimum principal stress σ_{min} along the tie's longitudinal cross section at the center. The 24-wire tie displays a slightly stronger compressive stress state upon pretension release than the 8-strand tie. The residual tensions averaged for all tendons are plotted in Figure 11 as a function of the relative distance to the center of the tie. The residual tensions are compared with their initial pretensions in this plot. Figure 12 further plots the ratio of the residual tension to the pretension for both ties. Again the 24-wire tie shows better retention of

the pretension than the 8-strand tie, and this is consistent with the fact that there is more interfacial area in the 24-wire tie for bonding with the concrete.

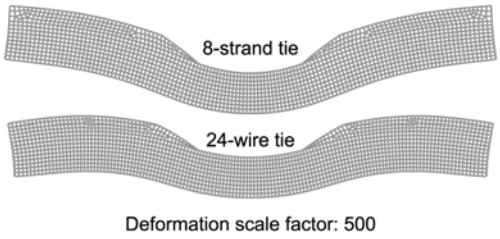

Figure 8. Predicted deformation profiles of the two concrete crossties upon pretension release.

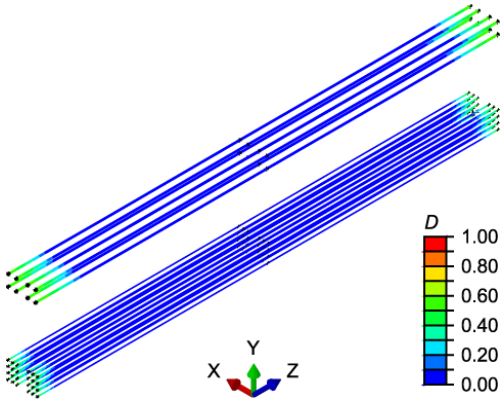

Figure 9. Predicted interface deterioration contours for the 8-strand and 24-wire ties after pretension release.

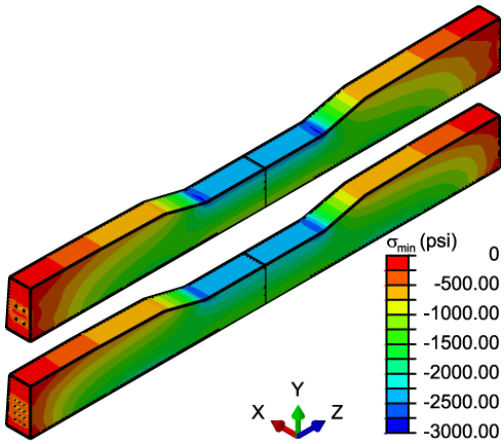

Figure 10. Predicted compressive stress state contours in concrete for the 8-strand and 24-wire ties after pretension release.

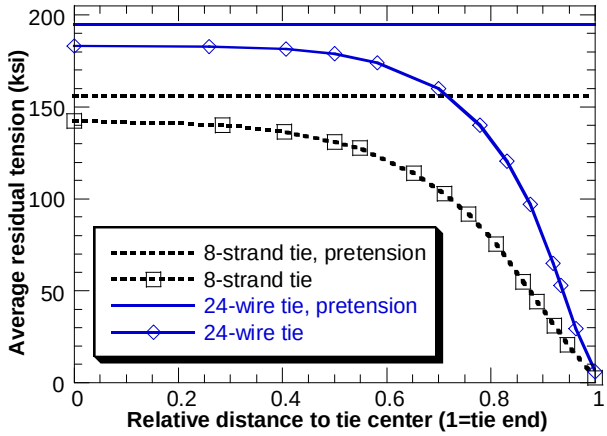

Figure 11. Predicted average residual tensions in the tendons as a function of the relative distance to the tie center.

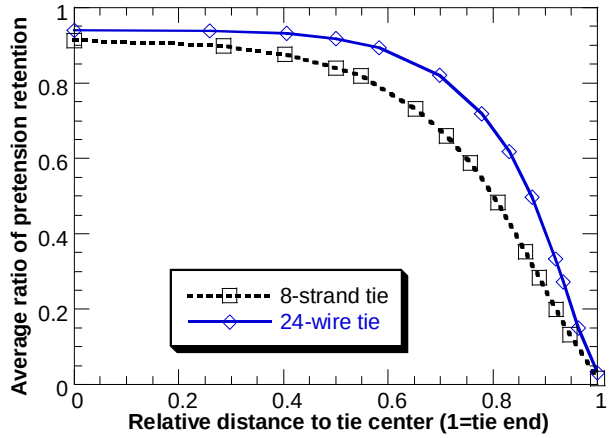

Figure 12. Predicted average ratios of retained pretensions as a function of the relative distance to the tie center.

4.2 Direct Rail Seat Loading

As illustrated in Figure 7, a pressure load increasing linearly to 50 ksi in one second is applied on a predefined rail seat area of about 22.55 inch^2 for the concrete ties and 19.375 inch^2 for the wood tie. The duration of the load is randomly selected. Under this pressure loading, tensile damages at the bases of both the 8-strand and the 24-wire concrete crossties are observed in the simulations. A concrete tie is considered damaged as the concrete tensile damage variable d_t reaches a substantial amount (greater than 0.1). On the other hand, compressive damage is observed on the rail seat of the wood tie as the compressive stress along the rail seat loading direction reaches its strength limit in that direction.

The vertical resultant forces acting on the rail seats are calculated for the quarter symmetric models and plotted in Figure 13(a) versus the corresponding displacements averaged over the predefined rail seat area. It is noted that the rail seat forces in this and subsequent plots account for only half of the typical railroad wheel loads. A rail seat displacement relative to the tie base is also calculated, and the resulting force-relative displacement relations are plotted in Figure 13(b) for the three ties. All curves are plotted up to the point of perceived tie failure as defined above. The 8-strand tie appears to be more susceptible to tensile cracking than the 24-wire tie, as evidenced by the lower rail seat force at failure (31.6 vs. 40.6 kips). As discussed, the wood tie fails with a different mechanism than that in the concrete ties; in addition, it presents a more compliant response overall and sustains a lower amount of rail seat force at failure (21.3 kips).

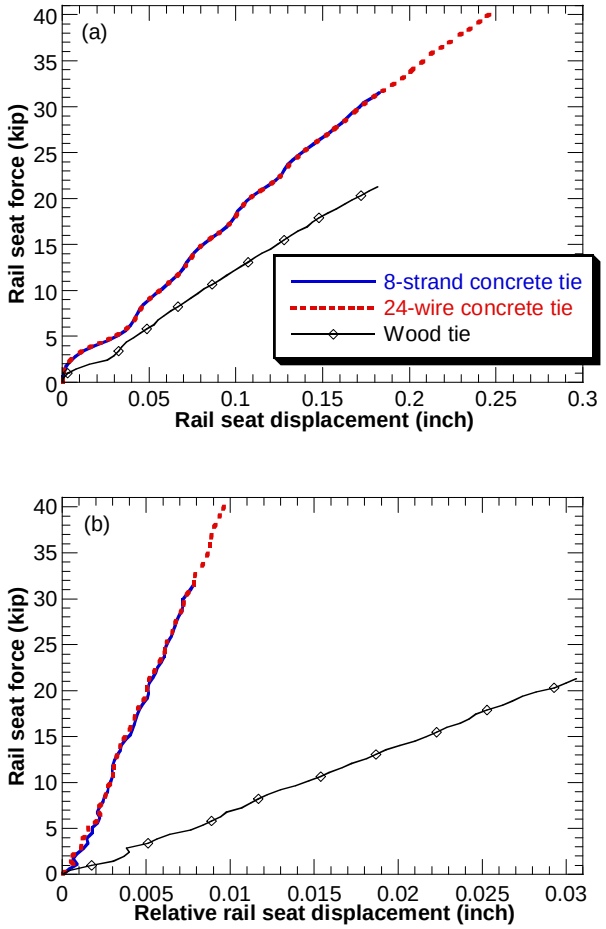

Figure 13. Rail seat force vs. (a) rail seat displacement and (b) rail seat displacement relative to tie base for the three railroad crossties.

5. CONCLUSIONS

This paper presents an FE analysis framework for individual concrete crossties that takes into account their macroscopic heterogeneity and material nonlinearity. In particular, the interfaces between the reinforcements and the concrete matrix are explicitly modeled and assigned bond-slip relationships. The FE method is able to predict the stress states in the two concrete ties with eight prestressing strands and twenty four prestressing wires, respectively, upon release of the pretensions in the tendons. The 24-wire tie shows better retention of the pretensions than the 8-strand tie, likely owing to the increased bonding surfaces between the wires and the concrete in the 24-wire tie.

A wood tie model following orthotropic elasticity and orthotropic stress failure criteria is also developed, and ballast and subgrade are included in modeling to provide support for the ties. Under a simplified rail seat pressure loading, both concrete ties appear to experience tensile cracking failure at the tie base, whereas the wood tie experiences compressive failure in the rail seats under sufficiently large rail seat forces. The 24-wire concrete tie fails at a larger rail seat force than the 8-strand concrete tie. Both concrete ties sustain larger rail seat forces than what the wood tie does upon tie failure.

The FE analysis framework can be further improved by modeling additional components such as rail fasteners to represent the rail-to-tie load transferring paths more accurately. Additional bond strength data will be sought for different tendon diameters and surface conditions. The FE modeling approach will also need to be verified or validated with experimental results.

6. ACKNOWLEDGEMENT

The work described in this paper was sponsored by the U.S. Federal Railroad Administration. Technical discussions with Mr. Michael Coltman, Dr. Ted Sussmann and Mr. John Choros are gratefully acknowledged.

7. References

1. A.N. Hanna, 1979: "State-of-the-art report on prestressed concrete ties for North American railroads," PCI Journal, September-October: 32-61.

2. National Transportation Safety Board, 2006: Railroad accident brief. NTSB/RAB-06/03.

3. H. Yu, D.Y. Jeong, 2010: "Finite element modeling of railroad concrete crossties – a preliminary study," Proceedings of International Conference on Railway Engineering, Beijing, pp. 277-282.

4. R., Gustavson, 2002: "Bond behavior of four types of strands in sleepers during release of prestress and loading," Chalmers University of Technology, Department of Structural Engineering, Report 02:14, Göteborg.

5. H. Yu, D.Y. Jeong, J. Choros, and T. Sussmann, "Finite element modeling of prestressed concrete crossties with ballast and subgrade support," Proceedings of the ASME 2011 International Design Engineering Technical Conferences & Computers and Information in Engineering Conference, August 29-31, 2011, Washington, DC, USA.

6. Dassault Systèmes Simulia Corp. ABAQUS Analysis User's Manual.
7. V.S. Gopalaratnam, S.P. Shah, 1985: "Softening response of plain concrete in direct tension," ACI Journal, Proceedings V. 82, No. 3, pp. 310-323.
8. A. Hillerborg, M. Modeer, P.E. Petersson, 1976: "Analysis of crack formation and crack growth in concrete by means of fracture mechanics and finite elements," Cem. Concr. Res. 6, pp. 773–782.
9. S. Popovics, 1970: "A review of stress-strain relationships for concrete," ACI Journal, Vol. 67, No. 14, pp. 243-248.
10. E. Thorenfeldt, A. Tomaszewicz, J.J. Jensen, 1987: "Mechanical properties of high-strength concrete and application in design," Proceedings of the Symposium "Utilization of High Strength Concrete," Stavanger, Norway, pp. 149-159.
11. M.P. Collins, Mitchell, D., 1991: *Prestressed Concrete Structures*, Prentice-Hall, New Jersey.
12. M. Elmorsi, M. Reza Kianoush, and W.K. Tso, 1998: "Nonlinear analysis of cyclically loaded reinforced concrete structures," ACI Structural Journal, Vol. 95, No. S66, pp. 725-739.
13. D. Palermo, F.J. Vecchio, 2003: "Compression field modeling of reinforced concrete subjected to reversed loading: formulation," ACI Structural Journal, Vol. 100, No. S64, pp. 616-625.
14. Lubliner, J., Oliver, J., Oller, S. and Oñate, E. 1989. A plastic-damage model for concrete. International Journal of Solids and Structures. Vol. 25:299–329.
15. Lee, J. and Fenves, G.L. 1998. Plastic-damage model for cyclic loading of concrete structures. Journal of Engineering Mechanics. Vol. 124, No. 8:892–900.
16. H. Abrishami, D. Mitchell, 1993: "Bond characteristics of pretensioned strand," ACI Materials Journal, Vol. 90, No. 3, pp. 228-235.
17. R. Gustavson, 2004: "Experimental studies of the bond response of three-wire strands and some influencing parameters," Materials and Structures, Vol. 37, No. 2, pp. 96-106.
18. Bergman, R., Cai, Z., Carll, C.G., Clausen, C.A., Dietenberger, M.A., Falk, R.H., Frihart, C.R., Glass, S.V., Hunt, C.G., Ibach, R.E., Kretschmann, D.E., Rammer, D.R., Ross, R.J., Stark, N.M., Wacker, J.P., Wang, X., White, R.H., Wiedenhoeft A.C., Wiemann, M.C., Zelinka, S.L., Wood handbook - Wood as an engineering material. General Technical Report FPL-GTR-190. Madison, WI: U.S. Department of Agriculture, Forest Service, Forest Products Laboratory: 508 p. 2010.
19. Indraratna, B., Salim, W. and Rujikiatkamjorn, C. 2007. Development and application of constitutive model for railway ballast. In: Yin, JH, Li, XS, Yeung, AT & Desai, CS (eds.), International Workshop on Constitutive Modelling, Hong Kong, pp. 685-696.
20. Q. Feng, X. Lei, S. Lian, 2010: "Ground vibration generated by high-speed train," Proceedings of International Conference on Railway Engineering, Beijing, pp. 379-384.
21. Dassault Systèmes Simulia Corp. ABAQUS Theory Manual.